Biomimetic Closed-loop Control of a Novel Soft Gastric Simulator Toward Emulating Antral Contraction Waves

Shahab Kazemi,[1] Ryman Hashem,[2] Martin Stommel,[3] Leo K. Cheng,[4] and Weiliang Xu,[1]

Abstract

Soft gastric simulators are in-vitro biomimetic modules that can reproduce the antral contraction waves (ACWs). Along with providing information concerning stomach contents, stomach simulators enable experts to evaluate the digestion process of foods and drugs. Traditionally, open-loop control approaches were implemented on stomach simulators to produce ACWs. Constructing a closed-loop control system is essential to improve the simulator's ability to imitate ACWs in additional scenarios and avoid constant tuning. Closed-loop control can enhance stomach simulators in accuracy, responding to various food and drug contents, timing, and unknown disturbances. In this paper, a new generation of anatomically realistic soft pneumatic gastric simulators is designed and fabricated. The presented simulator represents the antrum, the lower portion of the stomach where ACWs occur. It is equipped with a real-time feedback system to implement diverse closed-loop controllers on demand. All the details of the physical design, fabrication, and assembly process are discussed. Also, the measures taken for the mechatronics design and sensory system are highlighted in this paper. Through several implementation algorithms and techniques, three closed-loop controllers including model-based and model-free schemes are designed and successfully applied on the presented simulator to imitate ACWs. All the experimental outcomes are carefully analyzed and compared against the biological counterparts. It is demonstrated that the presented simulator can serve as a reliable tool and method to scrutinize digestion and promote novel technologies around the human stomach and the digestion process. This research methodology can also be utilized to develop other biomimetic and bioinspired applications.

Keywords: stomach simulator, closed-loop control, mechatronics design, soft actuator, pneumatic actuators, peristalsis

Introduction

Soft robotics has advanced various applications, such as biomimetic devices for emulating biological systems. This field aims to find a solution for problems that cannot be solved by current rigid mechanical design. The human body comprises different smooth muscles with intricate patterns of movements such as stretching, contraction, retraction, bending, twisting, and flexion. It is uncommon and challenging to mimic smooth muscle organs with traditional robotics techniques. Meanwhile, soft robotics' biomimicry branch focuses on replicating these complex motions with low-cost actuation using soft materials. Organs like the esophagus, heart, stomach, tongue, and intestine are examples of these smooth muscles that have received researchers' attention in the past few years.

For example, a soft biomimicry system simulating a human's tongue was designed and fabricated using silicon rubber. This artificial tongue could replicate human tongue deformations and interactions with surroundings.[1] The heart is another organ that researchers are interested in replicating its movement. There are various studies around employing soft robotic techniques to emulate the heart motion owing to its relatively simple pump-like function.[2-4] In another research, an artificial lung was developed to simulate the breathing action.[5] Silicon elastomer was used as the material because of its similarity to the mechanical properties of mammalian tissue and ease of fabrication. Driven et al., designed and developed an esophageal swallowing robot with an occlusive surface by using the same silicon elastomer material.[6] Another example of the biomimicking organ is the intestine, where the circular muscle is arranged annularly in its tract and performs occlusion by contraction and relaxation. Inspired by the human intestine, a crawling pneumatic soft endoscope was developed and successfully moved and extracted objects from rigid, flexible pipes.[7]

In addition, studies have been carried out about utilizing soft ring actuators to imitate the radial contraction of the wall of muscular organs like the stomach or bladder in recent years.[8] Soft ring actuators can expand and retract their inner diameter against the conduit according to the applied pressure, allowing material to be transported through the chamber. One noteworthy bioinspired application of ring actuators is peristaltic pumps,

[1] Department of Mechanical and Mechatronics Engineering, The University of Auckland, Auckland, New Zealand.
[2] Department of Medical Physics and Bioengineering, University College London, London, England.
[3] Department of Electrical & Electronic Engineering, Auckland University of Technology, Auckland, New Zealand.
[4] Auckland Bioengineering Institute, The University of Auckland, Auckland, New Zealand.

allowing for simple and secure transport of various media. [9,10] Ring actuators are also beneficial for simulating the motility function of internal organs like the stomach, esophagus, and intestine.[6,11,12]

In this study, we are particularly interested in accurately mimicking the stomach's mechanical function. Gastric simulators are biomimetic soft robots that can reproduce the peristaltic movement or the antral contraction waves (ACWs). ACWs are muscular advancing wavelike motions pushing food particles forward by continuous radial contractions. A stomach simulator capable of generating ACWs can serve the food and pharmaceutical industries for testing and analyzing newly developed foods and medicines.[13] In addition, they can provide an interface to test and validate advanced abdominal surgical tools. A few soft gastric simulators have recently been developed to emulate stomach activity.[13-15] However, these robots focused on the stomach's overall behavior, ignoring the geometry and contraction specifications of the antrum, where the largest occlusions and the ACWs occur. Soft gastric simulators' accurate position and motion control are demanding due to their continuum qualities. Like rigid-bodied robots, soft robots' control strategies are categorized into open-loop and closed-loop schemes. In our previous work, we developed a full soft gastric simulator that satisfies the specification of human stomach anatomy and motility to reproduce ACWs and the digestion phases during the actuation process.[16] However, due to the utilized open-loop approach, the generated ACWs were not dimensionally accurate, and the stomach content could affect the peristalsis. There was no way to tell if generated ACWs met the biological references requirement dimensionally. Open-loop control involves predicting the behaviour based on knowledge of the robot specifications without online feedback.[17-19] The dynamics model or trial and error processes are usually used to tune the open-loop control.

To date, open-loop control approaches have been implemented on stomach simulators to reproduce ACWs.[14,15,20,21] However, closed-loop control is required for the gastric simulator to improve its motility performance. The gastric simulators must meet specific dimensions regarding ACWs' amplitudes and frequencies (including pathologic conditions) in the stomach.[22,23] These measurements require precision control (only feasible with closed-loop methods), which is the main focus of this study. In addition, should stomach simulators be exposed to unknown stomach contents, open-loop approaches will fail to operate accurately. Cyclic loadings and unloading leading to soft tissues' hysteresis and creep is another factor that demands a closed-loop approach. In this study, using an online feedback system, we designed and implemented a closed-loop control over a soft gastric simulator's mechanical function for the first time.

Employing closed-loop controls to achieve an autonomous performance in soft robotics is a long-standing challenge. The soft bodies of the robots can prevent the use of conventional sensors.[24] As a solution, either the physical design or the sensor must be adapted for the control purpose.[25-27] An appropriate sensor for soft actuators must integrate into the compliant material and have enough motion range and accuracy to measure continuous posture changes. As an example, Felt *et al.* employed flexible sensors known as smart braids to control the contraction of the pneumatically driven McKibben muscles.[28] Case *et al.* implemented optimal proportional–integral–derivative (PID) feedback control (using an elastomer sensor) for bending angle control of elastomer beams.[29] In both studies, closed-loop control results were highly accurate compared to the relatively poor results of the open-loop approaches.

In addition, the modeling of soft actuators enhances their controllability and optimization prospects and formulates their behavior. With an adequate dynamic model, it is possible to design an efficient model-based controller. Compared to model-free controllers, model-based methods provide stability and improve transient performance and operability, shorten tuning time, and reduce rework in a much safer and quicker manner. Developing the dynamic model is the first step to designing and implementing the model-based control methods. Simple dynamic models for soft manipulators and actuators, including soft ring actuators, were formed using the first principles.[30-35] In the current work, after extracting an advanced dynamic model for a soft gastric simulator, we design and implement two nonlinear model-based closed-loop controllers for replicating ACWs. We also compare the results with a model-free controller to show the ability of model-based methods in the biomimicry application.

The remainder of this paper is organized as follows. Initially, a soft gastric simulator is developed to emulate ACWs. This robot comprises several ring-shaped soft pneumatic actuators (RiSPAs) installed inside a 3D-PDMS frame, which is anatomically accurate and moves like the actual stomach. For the first time, the presented stomach simulator is equipped with a real-time feedback system, which opens new windows to closed-loop related applications such as real-time mimicry, pathologic studies, and developing new medical and surgery tools. A nonlinear dynamic model representing the behavior of the soft gastric simulator is extracted. Then, two nonlinear model-based controllers are designed based on the presented model. The model-based and model-free controllers are implemented on the gastric simulator to replicate ACWs under full and empty stomach conditions. Eventually, all the experimental results are discussed in detail.

Physical development

The stomach is a distensible muscular hollow organ between the end of the esophagus and the beginning of the duodenum and helps digestion and regulates nutrition.[36] The stomach is heavily built of muscle tissues, arranged in three layers, running longitudinally, diagonally, and circularly as part of the stomach wall (Fig. 1a). Antrum is a hollow muscle that resides upstream from the pylorus and its junction of the pyloric sphincter to the duodenum (see Fig. 1b). The antrum rhythmically engages in ACWs (peristalsis), in response to the pacemaker's electrical stimulation to aid with the breaking down the food and mix it with gastric juices, which also serve to prepare the mixture. ACWs repeat with the frequency of three cycles per minute.[37-39]

[Figure 1 about here]

The average human adult stomach conduit geometry was previously conceptualized and a 2D geometry was extracted from its computerized tomography (CT) image.[40,41] The outer curves were initially developed in CAD software to achieve a 3D shape representing the stomach J-shape geometry. In the next step, several perpendicular lines were arranged in sequence between the drawn curves to recognize the midpoints. These lines agree with the diameters of the imaginary circles of the stomach, where the largest at the fundus is 80 mm to 100 mm, and the smallest at the pylorus is 5 mm to 15 mm.[42] Afterwards, a third curve that connects all the midpoints was drawn, forming the central curvature (see Fig. 1b). Eventually, the sweep function of the upper curvature around the central curvature was executed to create the stomach conduit (see Fig. 1c). In Fig. 1c, the bellows-driven actuators are distributed circularly and act inward against the conduit.[16]

The antrum is divided into three segments, the proximal antrum (PA), the middle antrum (MA), and the terminal antrum (TA) (see Fig. 1b). The gap between every two adjacent RiSPAs is 10 mm, the average width of ACWs.[23] These circular patterns are similar to already developed RiSPAs.[35] For each segment, four independent RiSPAs were considered. The number of bellows and the size of each segment is shown in Table 1. Note that the increasing occlusion of ACWs on approach to the pylorus and over time is attributed to the narrowing of the antrum from PA to TA (closer to the pylorus), rather than amplifying their amplitude.[23]

[Table 1 about here]

Figure 2 shows the schematic of the steps for fabricating the gastric simulator (More details in the fabrication process can be seen in our previous work[16]). The fabrication process (see Fig. 2) requires breaking 3D-printed molds after curing PDMS/Ecoflex. This process possibly damages the final product and needs multiple trials to avoid cracks, notches, and bubbles. In addition, to avoid building up the bubbles, we left the mold filled with Ecoflex/PDMS in a vacuum tank until all the bubbles disappeared. Also, as the system operates with pneumatic power, detecting the leakages and gluing the gaps was done through a long process.

[Figure 2 about here]

Mechatronics design

Sensory unit

A range sensor (VCNL4040) is employed to create a feedback system in the gastric simulator.[43] I^2C command format is simple for read and write operations between VCNL4040 and myRIO-1900 as the main board. NI myRIO has two I^2C pins (DIO14 and DIO15) with a maximum frequency of 400 kHz. This means myRIO can only directly provide feedback from two identical sensors with a similar slave address to avoid address conflicts. However, given the attributes of the design presented in Physical development section, it is required to work with multiple copies of the same I^2C device with the same slave address to reproduce under-control ACWs. In this case, an I^2C multiplexer, acting as a gatekeeper, is used to avoid address conflict.

The I^2C address of the multiplexer is 0x70 and can be connected to DIO14 and DIO15, and up to 8 VCNL4040 can be connected to it. By writing a single byte with the desired multiplexed output number (e.g., *i*th-sensor) to that port (can be adjusted from 0x70 to 0x77), each sensor was read. The schematic of sensor-multiplexer integration is shown in Fig. 3a.

In Fig. 3b the placement of the sensors on the outer frame is shown. Although one side of the gastric simulator was left open, the calibration was accomplished slowly due to its inconvenient physical shape. By starting from the fully vacuumed state and increasing the pressure, sensor counts (*cts*) changed.[43] After sensor counts were stabilized, displacements were measured, and the process repeated. From fully vacuumed state to zero pressure/vacuum the displacement was 6 mm. By increasing the pressure, another 12 mm displacement was

achieved (a total 18 mm course). To prevent from rapturing, displacements higher than 18 mm were not investigated. Finally, by using MATLAB (*cftool*) (Levenberg–Marquardt algorithm), the relationship between sensor counts (*cts*) and displacements (mm) was estimated as a function and used in LabVIEW script (see Fig. 3b).

[Figure 3 about here]

Electro-pneumatic unit

As indicated in Table 1, 66 bellows are employed to resemble the movements of the antrum in the presented design. However, the ultimate goal is to emulate ACWs, which is the contraction of each segment through the movement of bellows towards the center. This makes the design an over-actuated system. To avoid this, all bellows of each RiSPA are linked together through silicon pneumatic tubes as depicted in Fig. 2c. Through the pneumatic tubes, PA, MA, and TA were divided into four RiSPAs (a total of twelve RiSPAs). The system consists of positive and negative proportional valves for controlling both the contraction and the retraction states. Subsequently, 3/2-way solenoid valves were added to the design to switch between contraction and retraction states (to watch videos on how the RiSPA contracts and retracts, please see "Supplementary Movie S2 and S3" in our previous work [35]). To make the prototype portable, all the valves and switches were screwed on a platform (laser cut from an acrylic sheet) as shown in Fig. 4.

Each proportional valve has two communication terminals, one of which must be connected to an analog output pin in myRIO for transmitting command data. However, myRIO has only six analog outputs in total. Another 8 Pulse-width modulation (PWM) pins were used to cover a greater number of regulators. PWM signals can be transformed into analog signals using a simple resistor-capacitor (RC) low-pass filter integrated with an op-amp, coded in LabVIEW. The average voltage output increases as the duty cycle increases, and vice versa. This limits the number of regulators into fourteen (seven positive and seven negative valves).

Also, seven switch solenoid valves must be controlled by the same myRIO. The problem with solenoids was that they work with 24 VDC, and myRIO does not have such input/output. To control the solenoids, a Darlington transistor integrated into an IC called ULN2003A was employed (see Fig. 4). ULN2003A is a high voltage, high current Darlington array containing seven open collector common emitter pairs. This occupied another seven pins from myRIO.

Ideally, one sensor is required to control each RiSPA. However, due to the limitations in the multiplexer, transistor, and myRIO, maximum seven sensors can be installed. That is why two pairs of RiSPAs in PA and MA were connected to each other and two sensors were dedicated to each segment. Since the maximum occlusion ratio (80%) occurs in TA, three sensors were dedicated for this segment. It means that on the presented gastric simulator, seven sensors were attached (see Table 2). Integration of each sensor with a pair of proportional pressure and vacuum valves provided the ability of the closed-loop control of each RiSPA, and the combination of all those RiSPAs next to each other made an under-control gastric simulator.

[Figure 4 about here]

[Table 2 about here]

Experimental results

To create the coding platform for closed-loop controllers, LabVIEW interface was chosen. Instead of tuning signals manually and via an open-loop manner, a feedback system was built to reproduce ACWs. Fig. 5 is a brief illustration of the closed-loop implementation. Unlike open-loop stomach simulators that require a formula for the input pressure of each segment to reproduce ACWs,[14,16] the presented gastric simulator only needs to follow a predetermined peristalsis baseline through the closed-loop controller. A sinusoidal wave baseline was sent in a distinctive sequence through the antrum's segments, beginning with the first RiSPA in the PA and ending with the last RiSPA implanted in the TA. As depicted in Fig. 3a, a multiplexer operates to read several sensors upon necessity. Each sensor is in contact with a pneumatic unit, including a pressure regulator, vacuum regulator, and a switch solenoid valve. Fig. 5 shows essential algorithms to link all different functions autonomously to reproduce ACWs.

Fig. 5a illustrates the algorithm for the timing of ACW while traveling through different segments of the gastric simulator. Literature shows that the biological stomach has an average of three ACWs repeating every 20 seconds. The contractions start at PA and propagate downward to TA with a complete peristaltic cycle in 60

seconds.[39] Based on the elapsed time this algorithm establishes which sensor needs to be activated. With the help of the algorithm in Fig. 5b, the multiplexer sends commands to myRIO to activate the right sensor and its corresponding calibration. After creating the connection between sensors in a particularly timely manner, they must be linked to the right pneumatic unit. The neutral position of each bellows is 6 mm. The pressure regulator must be activated if the current sensor measurement is higher than 6 mm. The vacuum gets activated if smaller than 6 mm (see Fig. 5c).

[Figure 5 about here]

Modeling and control design

Since the presented soft gastric simulator is based on the RiSPA, a previously developed nonlinear model of the RiSPA was extended to match the new specifications in Tables 1 and 2.[44] The model was developed utilizing Euler-Lagrange mechanics and defining state variable vector as $\mathbf{x}(t) = [\mathbf{q}(t) \quad \dot{\mathbf{q}}(t)]^T \in R^{2n}$ and the input vector as $\mathbf{u}(t) = [\mathbf{u}_1(t), ..., \mathbf{u}_n(t), \mathbf{0}_{n\times 1}]^T$. The generalized coordinates vector was defined as $\mathbf{q}(t) = [r_1(t), ..., r_n(t), \theta_1(t), ..., \theta_n(t)]^T$ (see Fig. 6). The nonlinear model of the gastric simulator is obtained as:

$$\dot{\mathbf{x}}(t) = \mathbf{A}(\mathbf{x}(t))\mathbf{x}(t) + \mathbf{B}(\mathbf{x}(t))\mathbf{u}(t),$$
$$\mathbf{A}(\mathbf{x}(t)) = \begin{bmatrix} \mathbf{0}_{2n\times 2n} & \mathbf{I}_{2n\times 2n} \\ -\mathbf{M}^{-1}(\mathbf{x}(t))\mathbf{K} & -\mathbf{M}^{-1}(\mathbf{x}(t))\mathbf{C} \end{bmatrix}, \quad (1)$$
$$\mathbf{B}(\mathbf{x}(t)) = \begin{bmatrix} \mathbf{0}_{2n\times 2n} \\ \mathbf{M}^{-1}(\mathbf{x}(t)) \end{bmatrix},$$

in which:

$$\mathbf{M}(\mathbf{x}(t)) = \begin{bmatrix} \mathbf{m} & \mathbf{0}_{n\times n} \\ \mathbf{0}_{n\times n} & \mathbf{I}(\mathbf{x}(t)) \end{bmatrix}, \mathbf{K} = \begin{bmatrix} \mathbf{k_t} & \mathbf{0}_{n\times n} \\ \mathbf{0}_{n\times n} & \mathbf{k_\theta} \end{bmatrix},$$
$$\mathbf{C} = \begin{bmatrix} \mathbf{c_t} & \mathbf{0}_{n\times n} \\ \mathbf{0}_{n\times n} & \mathbf{c_\theta} \end{bmatrix}, \quad (2)$$

where $\mathbf{M}(\mathbf{x}(t))$, $\mathbf{K}$, and $\mathbf{C}$ are the inertia, stiffness, and the damping matrices of the gastric simulator, and m, k_t, k_θ, c_t, c_θ are calculated from Table 3.[44] $\mathbf{I}(\mathbf{x}(t)) = \text{diag}\,(I_p(r_1(t)), ..., I_p(r_n(t)))$ is a time-dependent matrix including nonlinear, time-variant scalars of $I_p(r_i(t))$, ($i = 1, ..., n$), representing inertia and geometry variations of RiSPAs.

$$I_x(r_i(t)) = \frac{mg}{4}(R^2 + r_i^2(t))\left(1 - \frac{\sin\alpha\cos\alpha}{\alpha}\right),$$
$$I_y(r_i(t)) = \frac{mg}{4}(R^2 + r_i^2(t))\left(1 + \frac{\sin\alpha\cos\alpha}{\alpha}\right) - \frac{2mg(R^3 - r_i^3(t))\sin\alpha}{3\alpha(R^2 - r_i^2(t))}, \quad (3)$$
$$I_p(r_i(t)) = I_x(r_i(t)) + I_y(r_i(t)) = m[0.5(R^2 + r_i^2(t)) - 0.38(\frac{R^3 - r_i^3(t)}{R^2 - r_i^2(t)})^2].$$

In above equations, $\alpha = \pi/n$, and n is the number of bellows in each RiSPA, depending on its segment (see Tables 1 and 2). Note that R in Eq. (3) is the half of the average diameter from Table 1.

[Table 3 about here]

[Figure 6 about here]

Three controllers were chosen to reproduce ACWs. Finite-horizon state dependent Riccati equation (FH-SDRE) was the first model-based controller to design. FH-SDRE is a nonlinear, optimal, finite-time controller. A finite-time controller can stabilize the dynamic system in any finite-time interval, while the state variables remain in a limited bound.[44,45] In our previous work, FH-SDRE was designed for a single RiSPA model and successfully implemented to mimic the contractions with different frequencies.[44] In this work, we also implement FH-SDRE, besides other controllers, for the entire gastric simulator to reproduce the ACWs. For the model represented in Eq. (1), the control law must minimize the finite-time quadratic cost function

$$J(\mathbf{x}(t),\mathbf{u}(t)) = \frac{1}{2}[\mathbf{x}^T(t_f)\mathbf{S}\mathbf{x}(t_f) + \int_0^{t_f}[\mathbf{x}^T(t)\mathbf{Q}\mathbf{x}(t) + \mathbf{u}^T(t))\mathbf{R}\mathbf{u}(t)]dt], \quad (4)$$

in which **Q** and **S** (state weighting matrices) are real symmetric positive semi-definite, and **R** (input weighting matrix) is a positive definite matrix. Utilizing the optimally necessary conditions, the control law is calculated as

$$\mathbf{u}(t) = -\mathbf{R}^{-1}\mathbf{B}^T(\mathbf{x}(t))\mathbf{P}(\mathbf{x}(t))\mathbf{x}(t), \quad (5)$$

where $P(\mathbf{x}(t))$ comes from the following differential equation:

$$-\dot{\mathbf{P}}(\mathbf{x}(t),t) = \mathbf{P}(\mathbf{x}(t), t)\mathbf{A}(\mathbf{x}(t)) + \mathbf{A}^T(\mathbf{x}(t))\mathbf{P}(\mathbf{x}(t), t) - \mathbf{P}(\mathbf{x}(t), t)\mathbf{B}(\mathbf{x}(t))\mathbf{R}^{-1}\mathbf{B}^T(\mathbf{x}(t))\mathbf{P}(\mathbf{x}(t), t) + \mathbf{Q}. \quad (6)$$

in which Eq. (6) was solved using the state transition matrix method.[45]

Feedback linearization (FL) is the next model-based controller designed to reproduce ACWs in the proposed gastric simulator. FL is a simple yet effective control strategy for nonlinear, complicated systems like compliant actuators. This controller algebraically cancels the model's nonlinearities and is employed in many engineering applications such as helicopters, robots, autonomous underwater vehicles, and industrial applications.[46-50] For the relatively complicated nonlinear model in Eq. (1), FL can be a relative strategy to turn the model into a linear time invariant (LTI) system. FL transforms the nonlinear model into an entirely or partially linear one so that simple classical or modern linear controllers can be applied.[51] Since Eq. (1) is presented as the controllability canonical form, an input-state linearization feedback controller was directly designed. Using the FL technique, the algebraic transformation,

$$\mathbf{u}(t) = -\mathbf{M}(\mathbf{x}(t))\mathbf{v}(\mathbf{x}(t)) + \mathbf{K}\mathbf{q}(t) + \mathbf{C}\dot{\mathbf{q}}(t), \quad (7)$$

was applied on Eq. (1). Note that $\mathbf{v}(\mathbf{x}(t))$ can be any linear state feedback controller. By inserting the input from Eq. (7) into the dynamic model, the nonlinear model transforms into the LTI system

$$\dot{\mathbf{x}}(t) = [\dot{\mathbf{q}}(t) \quad \mathbf{v}(\mathbf{x}(t))]^T. \quad (8)$$

The nonlinear dynamic model can be rewritten in linearized format as

$$\dot{\mathbf{x}}(t) = \mathbf{A}^* \mathbf{x}(t) + \mathbf{B}^* \mathbf{v}(\mathbf{x}(t))$$
$$= \begin{bmatrix}\mathbf{0}_{2n\times 2n} & \mathbf{I}_{2n\times 2n}\\ \mathbf{0}_{2n\times 2n} & \mathbf{0}_{2n\times 2n}\end{bmatrix}\begin{bmatrix}\mathbf{q}(t)\\ \dot{\mathbf{q}}(t)\end{bmatrix} + \begin{bmatrix}\mathbf{0}_{2n\times 2n}\\ \mathbf{I}_{2n\times 2n}\end{bmatrix}\mathbf{v}(\mathbf{x}(t)), \quad (9)$$

where $\mathbf{A}^* \in R^{4n\times 4n}$ and $\mathbf{B}^* \in R^{4n\times 2n}$ are LTI matrices representing the new linearized form. Thus, for the obtained linearized model (9), the linear quadratic regulator (LQR), as an optimal, linear controller, can be designed. To design the LQR for the LTI system, the static gain **k** must be calculated in a way that the control law, $\mathbf{v}(\mathbf{x}(t)) = -\mathbf{k}\,\mathbf{x}(t)$, minimizes the infinite quadratic cost function,

$$J(\mathbf{x}(0),\mathbf{v}(.)) = \frac{1}{2}\int_0^{\infty}[\mathbf{x}^T(t)\mathbf{Q}\mathbf{x}(t) + \mathbf{v}^T(\mathbf{x}(t))\mathbf{R}\mathbf{v}(\mathbf{x}(t))]dt, \quad (10)$$

where $\mathbf{k} = -\mathbf{R}^{-1}\mathbf{B}^T\mathbf{P}$, and **P** comes from the following algebraic equation.

$$\mathbf{A}^{*T}\mathbf{P} + \mathbf{P}\mathbf{A}^* - \mathbf{P}\mathbf{B}^*\mathbf{R}^{-1}\mathbf{B}^{*T}\mathbf{P} + \mathbf{Q} = 0. \quad (11)$$

The third controller is a model-free PD controller. Without of any modeling, $\mathbf{u}(t) = -\mathbf{k_p}\,\mathbf{x}(t) - \mathbf{k_d}\dot{\mathbf{x}}(t)$, is the control law. PD's control gains and weighting matrices for both the FH-SDRE and FL were tuned manually until the state variables met the control aims through numerical simulation (MATLAB).

Flowcharts in Fig. 7(a-b) illustrate the steps taken for real-time numerical simulations. From the simulation, control gains were calculated $\mathbf{k_p} = 5$ and $\mathbf{k_d} = 1$ and the weighting matrices were opted $\mathbf{Q} = 100 \times \mathbf{I}_{2n\times 2n}$, $\mathbf{S} = 100 \times \mathbf{I}_{2n\times 2n}$, and $\mathbf{R} = \mathbf{I}_{n\times n}$. Fig. 7c illustrates the block diagram for implementing the controllers in LabVIEW interface. It begins with defining the peristalsis trajectory as the baseline. Since the amplitude of ACWs does not alter over the central antral curvature,[23] the peristalsis baseline was defined as a single trajectory. The frequency of the peristalsis trajectory was 0.05 Hz, and the amplitude and offset were chosen 4 mm and 6 mm to be consistent with the biology references and the neutral position.

[Figure 7 about here]

Results and discussion

All specifications of ACWs like width, lifespan, velocity, frequency, and contraction ratios, can be altered and generated by changing the peristalsis baseline. The three designed controllers were implemented on the presented gastric simulator, following the logic in Fig. 7c. Fig. 8 illustrates tracking of the peristalsis trajectory using the proposed closed-loop controllers. It shows that ACWs are closely followed by the closed-loop controllers despite having a totally soft module. Fig. 8(a-c) illustrates the propagation of ACWs in PA, MA, and TA segments (to see a video on how the RiSPAs contract and retract, please see "Supplementary Video S1" in our previous publication[16]). Fig. 8d depicts all three segments of the gastric simulator together to imitate ACWs with a continuous actuation every 20 seconds (also see Fig. 2a). The peristaltic contraction of the robot exhibits a similar pattern to the behavior of a human stomach. The results validate that the presented gastric simulator can closely emulate the biological ACWs through closed-loop control. The fluctuations in Fig. 8 occur due to the spring-like nature of the actuators. Since bellows are made of viscoelastic material, they tend to restore themselves once the pressure is discharged. On the other hand, in the closed-loop system implementations, there are delays between two consecutive feedbacks. Due to these delays, the bellows restore themself instantly at each time step until the next feedback arrives, which results in fluctuations. However, since they are minimal against the ACWs trajectory, we ignored them during the experiments.

Table 4 presents quantitative differences between the experimental results of three proposed closed-loop control methods. These differences fall under the categories of precision control, root-mean-square error (RMSE), and control effort (control norm). In Table 4, the values for PA, MA, and TA are the average of two, two, and three RiSPAs, respectively. The experimental results were repeated several times and were mostly the same. From the experimental data, it can be concluded that model-based control methods outperform the PD in the presented gastric simulator. While designing a PD controller is more straightforward, its response to the natural variations of the soft system is relatively weak. Table 4 also suggests that although FL and FH-SDRE successfully track the peristalsis trajectory, they have some dissimilarities.

The RMSE and control norm in FL were higher than FH-SDRE. This was due to having nonlinear terms in FL's control law. While in FH-SDRE, there are nonlinear terms in the control law, the control gains were calculated based on nonlinearities. However, the control gains in FL came from the linearized model of (9). Meanwhile, since in the FH-SDRE, the control gains adapt themselves during the tracking process in real time (time variable control gain (see Eq. (6)), the accuracy performance was 36.5% better than FL. In the sense of control norm, PD sacrificed its accuracy for its control effort, which is not desirable in this application. The FH-SDRE consumed less control effort than FL (18.83% less control effort). The reason can be found in its optimal nature. While both of them employed optimal conditions, the model employed to design the FH-SDRE (Eq. (1)) is more accurate than that of FL (Eq. (9)). That is why the generated control gains were in more harmony with the physical setup and led to consuming less energy to achieve more acceptable accuracy.

[Figure 8 about here]

[Table 4 about here]

In order to show the ability of the controllers and the presented gastric simulator to track different trajectories, we repeated the previous experiment with a sawtooth trajectory while having the same frequency and amplitude as ACWs (see Fig. 9). It is shown that the control system can track the sawtooth trajectory suitably. The tendency of the results is consistent with the ACW tracking experiment. The RMSE for FH-SDRE, FL, and PD is calculated at 0.79 mm, 1.41 mm, and 1.92 mm, respectively.

[Figure 9 about here]

Another experiment was designed to investigate the effect of food content on the peristalsis under closed-loop controllers. Due to its similarity to chyme, a honey-like fluid made of a commercial food thickener is introduced to the gastric simulator as the food content. The prepared mix was injected into three balloons in quantities of 40 ml, 60 ml, and 80 ml (see Fig. 10a). These numbers were chosen to be a reasonable content volume against the robot's volume of roughly 335.5 ml. Note that inserting the balloons and removing them from the lumen of the robot was done carefully to avoid damaging the soft layer or creating hidden holes by deforming the bellows. The peristalsis trajectory tracking, including stomach content, was experimentally conducted, with similar control gains as those in the previous experiment. To maintain the RMSE small, the controllers automatically increased the control effort to compensate for the force applied by the balloons. Fig. 10b illustrates that all the controllers increased their control effort to maintain acceptable tracking performance. Note that despite the disturbance from the balloons and their texture, the soft actuators followed the peristalsis trajectory, the same as Fig. 8. Without the closed-loop system, the peristalsis would be considerably disturbed due to the lack of real-

time feedback. Also, all inputs must be re-adjusted for the open-loop approach to deal with an external disturbance like food content. This is another advantage of utilizing a closed-loop controller to replicate the peristalsis over open-loop approaches.

[Figure 10 about here]

Conclusion and future work

In this paper, a soft robotic gastric simulator, which dynamically and anatomically resembles the antrum, was developed to emulate ACWs. For the first time, the human gastric motility function was emulated under closed-loop control in a soft gastric simulator. It was built based on the RiSPA actuation, where an array of bellows generates radial contractions. After the design and fabrication of physical features, a mechatronics design was carried out to replicate the motility functions of the stomach. Besides the pneumatic unit, a feedback system was developed to implement closed-loop controllers. Two model-based controllers (FL and FH-SDRE) were designed and implemented on the presented gastric simulator to emulate the peristalsis. Under the closed-loop control, the presented simulator reproduced the peristalsis observed in the human antrum. A PD controller was also implemented on the robot to highlight the advantages of model-based controllers. All the proposed controllers' data were analyzed and compared thoroughly. Also, a honey-like mix was introduced in different volumes to the simulator as food contents. It was demonstrated that under closed-loop control, the robot successfully reproduced ACWs regardless of the external disturbances and design imperfections. The presented gastric simulator can emulate the human stomach's physiological motilities to advance digestion research. In the future, instead of using off-the-shelf sensors, embedded stretchable sensors can be replaced. These sensors can measure the contraction or the applied forces. With the presented closed-loop system, amplifying the human's stomach movements as trajectories and feeding them to the stomach simulator, as the baseline, will be feasible (at the moment, however, we are unable to noninvasively capture and amplify the stomach movement to generate the baseline). Doing so enables us to emulate each person's motility function in real time. It will aid in studying the reaction of digestive motility to different food contents and drugs.

Acknowledgment

The work presented in this paper was funded by the Riddet Institute, a centre of research excellence, New Zealand.

References

1. Lu X, Xu W, Li X. A soft robotic tongue—mechatronic design and surface reconstruction. IEEE ASME Trans Mechatron. 2017 Sep 4;22(5):2102-10.

2. Roche ET, Wohlfarth R, Overvelde JT, *et al*. A bioinspired soft actuated material. J Adv Mater. 2014 Feb;26(8):1200-6.

3. Schumacher CM, Loepfe M, Fuhrer R, Grass RN, Stark WJ. 3D printed lost-wax casted soft silicone monoblocks enable heart-inspired pumping by internal combustion. Rsc Advances. 2014;4(31):16039-42.

4. Cohrs NH, Petrou A, Loepfe M, *et al*. A soft total artificial heart—first concept evaluation on a hybrid mock circulation. Artif Organs. 2017 Oct;41(10):948-58.

5. Ranunkel O, Güder F, Arora H. Soft robotic surrogate lung. ACS Applied Bio Materials. 2019 Mar 8;2(4):1490-7.

6. Dirven S, Chen F, Xu W, *et al*. Design and characterization of a peristaltic actuator inspired by esophageal swallowing. IEEE ASME Trans Mechatron. 2013 Aug 28;19(4):1234-42.

7. Li G, Qiu W, Wen H, *et al*. Development of an Earthworm-Based Intestinal Soft Robot Equipped with a Gripper. Machines. 2022 Nov 10;10(11):1057.

8. Chen F, Dirven S, Xu W, *et al*. Large-deformation model of a soft-bodied esophageal actuator driven by air pressure. IEEE ASME Trans Mechatron. 2016 Sep 21;22(1):81-90.

9. Esser F, Steger T, Bach D, *et al*. Development of novel foam-based soft robotic ring actuators for a biomimetic peristaltic pumping system. In: Biomimetic and Biohybrid Systems: 6th International Conference, Living Machines 2017, Stanford, CA, USA, July 26–28, 2017, Proceedings 6 2017 (pp. 138-147). Springer International Publishing.

10. Ashigaki K, Iwasaki A, Hagiwara D, *et al*. Considering mixing process of rocket solid propellant using mixing transport device simulating peristaltic movement of intestinal tract. In: 2018 7th IEEE International Conference on Biomedical Robotics and Biomechatronics (Biorob) 2018 Aug 26 (pp. 1291-1296). IEEE.

11. Appiah C, Arndt C, Siemsen K, *et al*. Living materials herald a new era in soft robotics. J Adv Mater. 2019 Sep;31(36):1807747.

12. Dominy NJ, Davoust E, Minekus M. Adaptive function of soil consumption: an in vitro study modeling the human stomach and small intestine. J Exp Biol. 2004 Jan 15;207(2):319-24.

13. Condino S, Harada K, Pak NN, *et al*. Stomach simulator for analysis and validation of surgical endoluminal robots. Appl Bionics Biomech. 2011 Jan 1;8(2):267-77.

14. Dang Y, Liu Y, Hashem R, *et al*. SoGut: A soft robotic gastric simulator. Soft robot. 2021 Jun 1;8(3):273-83.

15. Li Y, Fortner L, Kong F. Development of a Gastric Simulation Model (GSM) incorporating gastric geometry and peristalsis for food digestion study. Food Res Int. 2019 Nov 1;125:108598.

16. Hashem R, Kazemi S, Stommel M, *et al*. SoRSS: A Soft Robot for Bio-Mimicking Stomach Anatomy and Motility. Soft Robot. 2022 Nov 7;10(3):504-516.

17. Thuruthel TG, Falotico E, Renda F, *et al*. Model-based reinforcement learning for closed-loop dynamic control of soft robotic manipulators. IEEE Trans Robot. 2018 Nov 11;35(1):124-34.

18. Marchese AD, Rus D. Design, kinematics, and control of a soft spatial fluidic elastomer manipulator. Int J Rob Res. 2016 Jun;35(7):840-69.

19. Farrow N, Correll N. A soft pneumatic actuator that can sense grasp and touch. In: 2015 IEEE/RSJ International Conference on Intelligent Robots and Systems (IROS) 2015 Sep 28 (pp. 2317-2323). IEEE.

20. Chen L, Xu Y, Fan T, *et al*. Gastric emptying and morphology of a 'near real'in vitro human stomach model (RD-IV-HSM). J Food Eng. 2016 Aug 1;183:1-8.

21. Kozu H, Nakata Y, Nakajima M, *et al*. Development of a human gastric digestion simulator equipped with peristalsis function for the direct observation and analysis of the food digestion process. Food Sci Technol Res. 2014;20(2):225-33.

22. Pal A, Brasseur JG, Abrahamsson B. A stomach road or "Magenstrasse" for gastric emptying. J Biomech. 2007 Jan 1;40(6):1202-10.

23. Kwiatek MA, Steingoetter A, Pal A, *et al.* Quantification of distal antral contractile motility in healthy human stomach with magnetic resonance imaging. J Magn Reson Imaging: An Official Journal of the International Society for Magnetic Resonance in Medicine. 2006 Nov;24(5):1101-9.

24. Gerboni G, Diodato A, Ciuti G, *et al*. Feedback control of soft robot actuators via commercial flex bend sensors. IEEE ASME Trans Mechatron. 2017 Apr 28;22(4):1881-8.

25. Thieffry M, Kruszewski A, Guerra TM, *et al*. Trajectory tracking control design for large-scale linear dynamical systems with applications to soft robotics. IEEE Trans Control Syst Technol. 2019 Dec 9;29(2):556-66.

26. Scharff RB, Fang G, Tian Y, *et al*. Sensing and reconstruction of 3-d deformation on pneumatic soft robots. IEEE ASME Trans Mechatron. 2021 May 7;26(4):1877-85.

27. Campisano F, Caló S, Remirez AA, *et al.* Closed-loop control of soft continuum manipulators under tip follower actuation. Int J Rob Res. 2021 Jun;40(6-7):923-38.

28. Felt W, Chin KY, Remy CD. Smart braid feedback for the closed-loop control of soft robotic systems. Soft robot. 2017 Sep 1;4(3):261-73.

29. Case JC, White EL, Kramer RK. Sensor enabled closed-loop bending control of soft beams. Smart Mater Struct. 2016 Mar 14;25(4):045018.

30. Dang Y, Devaraj H, Stommel M, *et al*. Experimental investigation into the dynamics of a radially contracting actuator with embedded sensing capability. Soft robot. 2020 Aug 1;7(4):478-90.

31. Uppalapati NK, Krishnan G. Towards pneumatic spiral grippers: Modeling and design considerations. Soft robot. 2018 Dec 1;5(6):695-709.

32. Mustaza SM, Elsayed Y, Lekakou C, *et al*. Dynamic modeling of fiber-reinforced soft manipulator: A visco-hyperelastic material-based continuum mechanics approach. Soft robot. 2019 Jun 1;6(3):305-17.

33. Chen W, Xiong C, Liu C, *et al.* Fabrication and dynamic modeling of bidirectional bending soft actuator integrated with optical waveguide curvature sensor. Soft robot. 2019 Aug 1;6(4):495-506.

34. Dang Y, Stommel M, Cheng LK, *et al*. A soft ring-shaped actuator for radial contracting deformation: Design and modeling. Soft robot. 2019 Aug 1;6(4):444-54.

35. Hashem R, Kazemi S, Stommel M, *et al*. A biologically inspired ring-shaped soft pneumatic actuator for large deformations. Soft robot. 2022 Aug 1;9(4):807-19.

36. Wilson RL, Stevenson CE. Anatomy and physiology of the stomach. In: Shackelford's Surgery of the Alimentary Tract, 2 Volume Set 2019 Jan 1 (pp. 634-646). Elsevier.

37. Mahadevan V. Anatomy of the stomach. Surgery (Oxf). 2014 Nov 1;32(11):571-4.

38. Soybel DI. Anatomy and physiology of the stomach. Surg Clin North Am. 2005 Oct 1;85(5):875-94.

39. Cheng LK, O'Grady G, Du P, *et al*. Gastrointestinal system. Wiley Interdiscip Rev Syst Biol Med. 2010 Jan;2(1):65-79.

40. Hashem R, Xu W, Stommel M, *et al*. Conceptualisation and specification of a biologically-inspired, soft-bodied gastric robot. In: 2016 23rd International Conference on Mechatronics and Machine Vision in Practice (M2VIP) 2016 Nov 28 (pp. 1-6). IEEE.

41. Du P, O'Grady G, Cheng LK, *et al*. A multiscale model of the electrophysiological basis of the human electrogastrogram. Biophys J. 2010 Nov 3;99(9):2784-92.

42. Ferrua MJ, Singh RP. Understanding the fluid dynamics of gastric digestion using computational modeling. Procedia Food Sci. 2011 Jan 1;1:1465-72.

43. Kazemi S, Hashem R, Stommel M, *et al*. Experimental Study on the Closed-Loop Control of a Soft Ring-Shaped Actuator for Gastric Simulator. IEEE ASME Trans Mechatron. 2022 Jan 4;27(5):3548-58.

44. Kazemi S, Stommel M, Cheng LK, *et al*. Finite-Time Contraction Control of a Ring-Shaped Soft Pneumatic Actuator Mimicking Gastric Pathologic Motility Conditions. Soft Robot. 2023 Apr 1;10(2):221-33.

45. Nekoo SR. Tutorial and review on the state-dependent Riccati equation. J Appl Nonlinear Dyn. 2019 Jun 1;8(2):109-66.

46. Mercorelli P. Robust feedback linearization using an adaptive PD regulator for a sensorless control of a throttle valve. Mechatronics (Oxf). 2009 Dec 1;19(8):1334-45.

47. Kazemi S, Geranmehr B, Nekoo SR. Finitary optimal gain for diving control of AUVs via input-state linearization. In: 2017 5th RSI international conference on robotics and mechatronics (ICRoM) 2017 Oct 25 (pp. 292-297). IEEE.

48. Geranmehr B, Khanmirza E, Kazemi S. Trajectory control of aggressive maneuver by agile autonomous helicopter. Proc Inst Mech Eng G J Aerosp Eng. 2019 Mar;233(4):1526-36.

49. Kazemi S, Rafee Nekoo S. Robust finite-time feedback linearization control of robots: theory and experiment. J Braz Soc Mech Sci. 2018 Aug;40:1-1.

50. Lee D, Jin Kim H, Sastry S. Feedback linearization vs. adaptive sliding mode control for a quadrotor helicopter. Int J Control Autom Syst. 2009 Jun;7:419-28.

51. Slotine JJ, Li W. Applied nonlinear control. Englewood Cliffs, NJ: Prentice Hall; 1991 Jan.

Address correspondence to:
Professor Weiliang Xu
Department of Mechanical and Mechatronics Engineering
The University of Auckland
20 Symonds Street
Auckland 1142
New Zealand
E-mail: p.xu@auckland.ac.nz

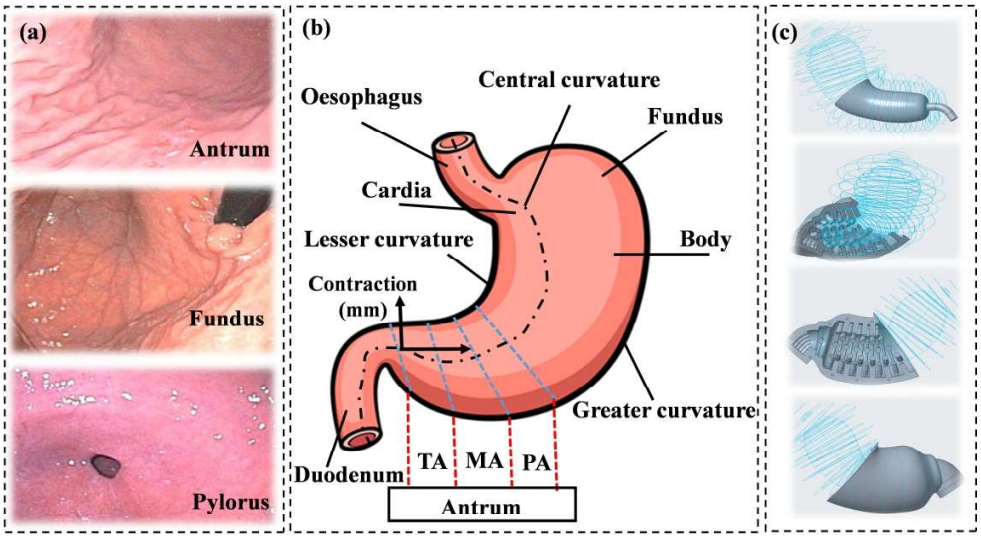

Fig. 1. (a) Internal view of the stomach muscles with different textures. **(b)** The stomach has five regions, including the gastroesophageal junction (cardia), the fundus, the body (corpus), the antrum, and the pylorus.37,38 Note that despite the blue-dashed lines, the antrum is not easily distinguishable with the boundary between the corpus and the antrum difficult to visually delineate. Also, the schematic of the stomach shows different sections of the antrum. **(c)** 3D projections of the designed stomach simulator in CAD. Different projections of the CAD design of the inner mold for the conduit and the outer mold with bellows.

1005x547mm (96 x 96 DPI)

Table 1. The physical characteristics of the gastric simulator. The sizes are based on the outer layer of the gastric simulator made of PDMS.

Section	No. of bellows	Central curve length	Avg. diameter
Proximal antrum	18	40 mm	62 mm
Middle antrum	24	40 mm	59 mm
Terminal antrum	24	40 mm	58 mm
Total	66	120 mm	59.6 mm

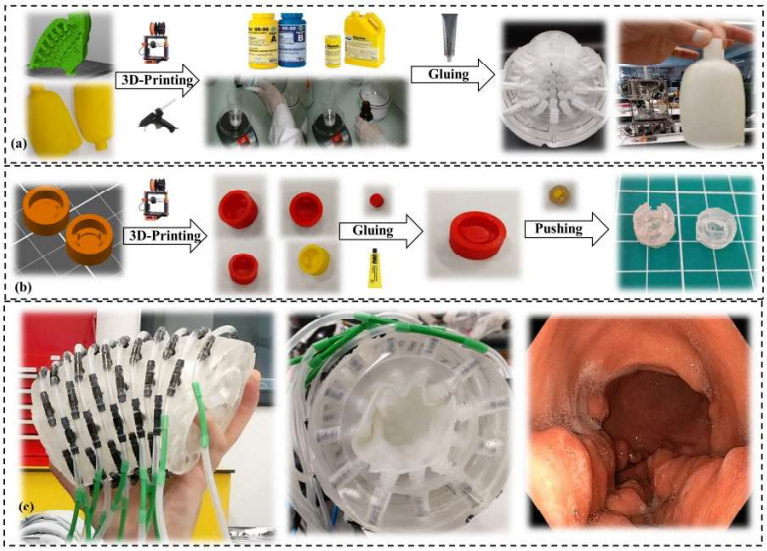

Fig. 2. (a) 3D-design and print of the molds. Hot glue gun was used to seal the seams between the 2-pieces molds when the uncured elastomer (Ecoflex 00-30 and Slacker; Smooth-on, Inc.), was poured inside the assemblies. Elastomer mix were Ecoflex (1A:1B) and PDMS (1 curing agent:10 PDMS (Sylgard 184 silicone elastomer; DOW)) similar to previous work.[16,35] Slacker™ was added to Ecoflex mix to change the "feel" of the silicone rubber to a softer and more "flesh-like" material by 0.5. Sil-Poxy™ (Sil-Poxy; Smooth-on, Inc.) is an adhesive for bonding different soft parts together. **(b)** The process of producing sensor caps, in which PDMS was used as it is clearer than Ecoflex. **(c)** The final assembled/sealed gastric simulator showing the side and front (PA), the pneumatic tubes and fittings, and the comparison with an actual antrum.

338x190mm (300 x 300 DPI)

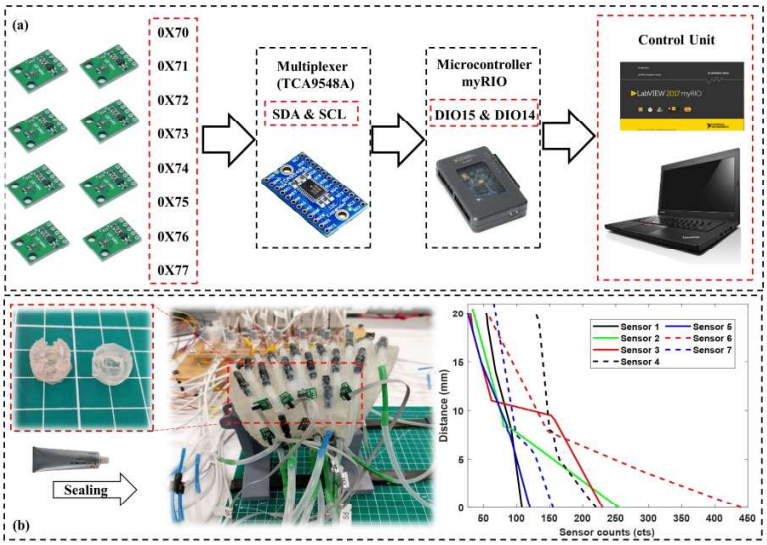

Fig. 3. (a) The connection between VCNL4040, multiplexer, myRIO and the PC. VCNL4040 has a unique device address (slave address), 0x60 (HEX), so myRIO can choose which devices will be communicating through two sensor wires. The two wires are the serial clock (SCL) and serial data (SDA). The SCL line is the clock signal that synchronizes the data transfer between the devices on the I^2C bus and is generated by the master device, and the other line, SDA, carries the data. TCA9548A multiplexer (outside of the gastric simulator attached to myRIO through wires) can get up to eight same slave address I^2C sensors communicating to one microcontroller. **(b)** The attachment of the sensors on the top of sensor caps and their placement on the gastric simulator using silicon glue, and the calibration graph of the sensors. Note that a lowpass filter is added to reduce the sensor noises.

338x190mm (300 x 300 DPI)

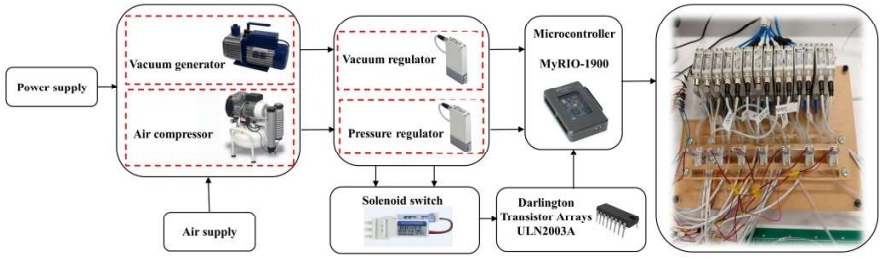

Fig. 4. Schematic of the electro-pneumatic system. For the pressurized state, electro-pneumatic regulators (ITV0030, SMC), pressure regulator, and for the vacuum state electronic vacuum regulators (ITV0090, SMC), vacuum regulator, are used. The relationship between the input signal and the pressure/vacuum outputs is linear in both ITV0030 and ITV0090. The pressure range for the vacuum and pressure regulators is -100 and 500 kPa, respectively. For the switching state, a micro-3-port solenoid valve (005 series, KOGANEI) is use. NI myRIO acts as an integration unit to merge the sensory and pneumatic parts into one entity and process all the data, controller, and feedback through LabVIEW scripts.

338x190mm (300 x 300 DPI)

Table 2. The mechatronics design for the gastric simulator.

Section	RiSPAs	Paired RiSPAs	Sensors	Regulators
Proximal antrum	4	2	2	4
Middle antrum	4	2	2	4
Terminal antrum	4	1	3	6
Total	12	5	7	14

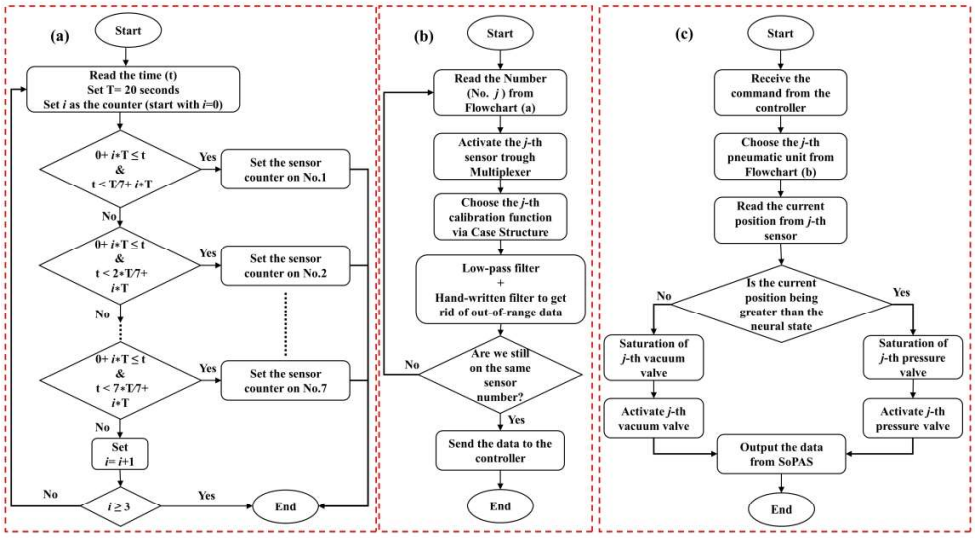

Fig. 5. The algorithms of **(a)** sequencing, **(b)** multiplexer and sensor readings, (c) and their connection to the regulator commands. In Electro-pneumatic unit section, it was explained that each regulator and solenoid was connected to a specific myRIO pin, including analog output, PWM, and digital input/output. Solenoid acts as a switch between pressure and vacuum regulators.

338x190mm (300 x 300 DPI)

Table 3. The physical characteristic for each RiSPA (see Fig. 6a).[44]

Description	Parameter	Value	Unit
Translational stiffness	k_t	0.65	$N.mm^{-1}$
Angular stiffness	k_θ	0.68	$N.mm.rad^{-1}$
Translational damping coefficient	c_t	1	$N.s.mm^{-1}$
Angular damping coefficient	c_θ	1.9	$N.s.rad^{-1}$
Mass of *i*th-SPA	m	1	gr

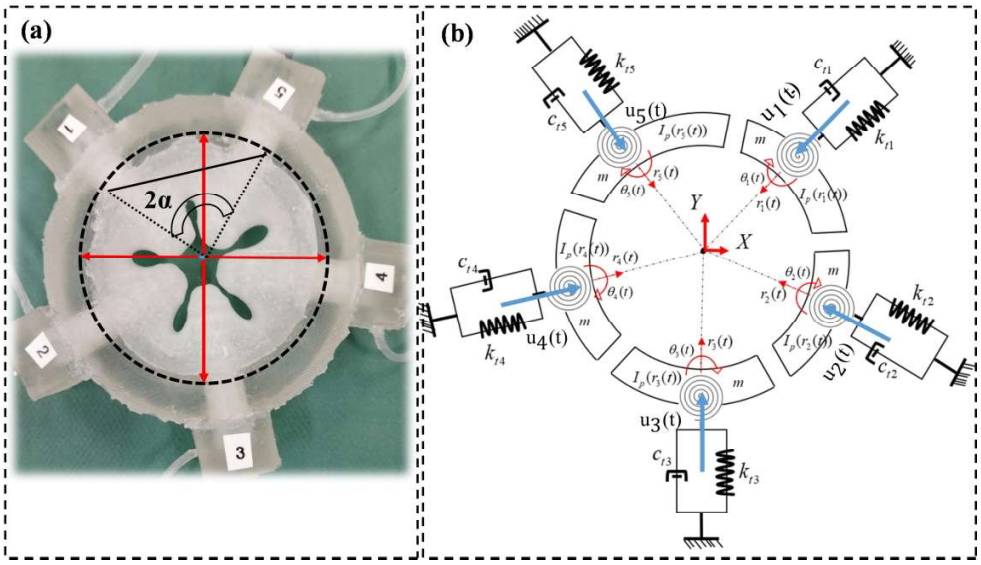

Fig. 6. (a) The sample of a RiSPA with five bellows. For the bellows' arrangement, they are scattered over the conduit uniformly without colliding.[16] The angle between the bellows is "2α=360" /"n," where n is the number of bellows in a RiSPA. **(b)** The schematics of a RiSPA and its model characteristics, where $r_i(t)$ and $\theta_i(t)$,(i= 1,...,n)," are radial and lateral movements of the ith-bellows in the cross-section plane.

806x460mm (96 x 96 DPI)

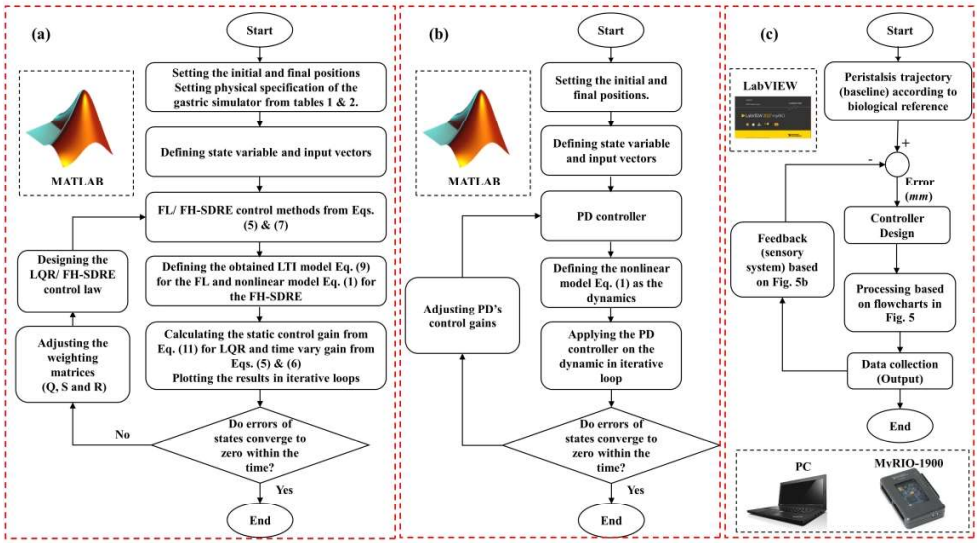

Fig. 7. (a) The flowchart of the numerical simulation (regulation process) to determine the weighting matrices for both the FL and FH-SDRE. **(b)** The flowchart of the numerical simulation (regulation process) to determine the control gains for the PD. **(c)** The implementation logic (block diagram) of the controllers on the presented gastric simulator.

338x190mm (300 x 300 DPI)

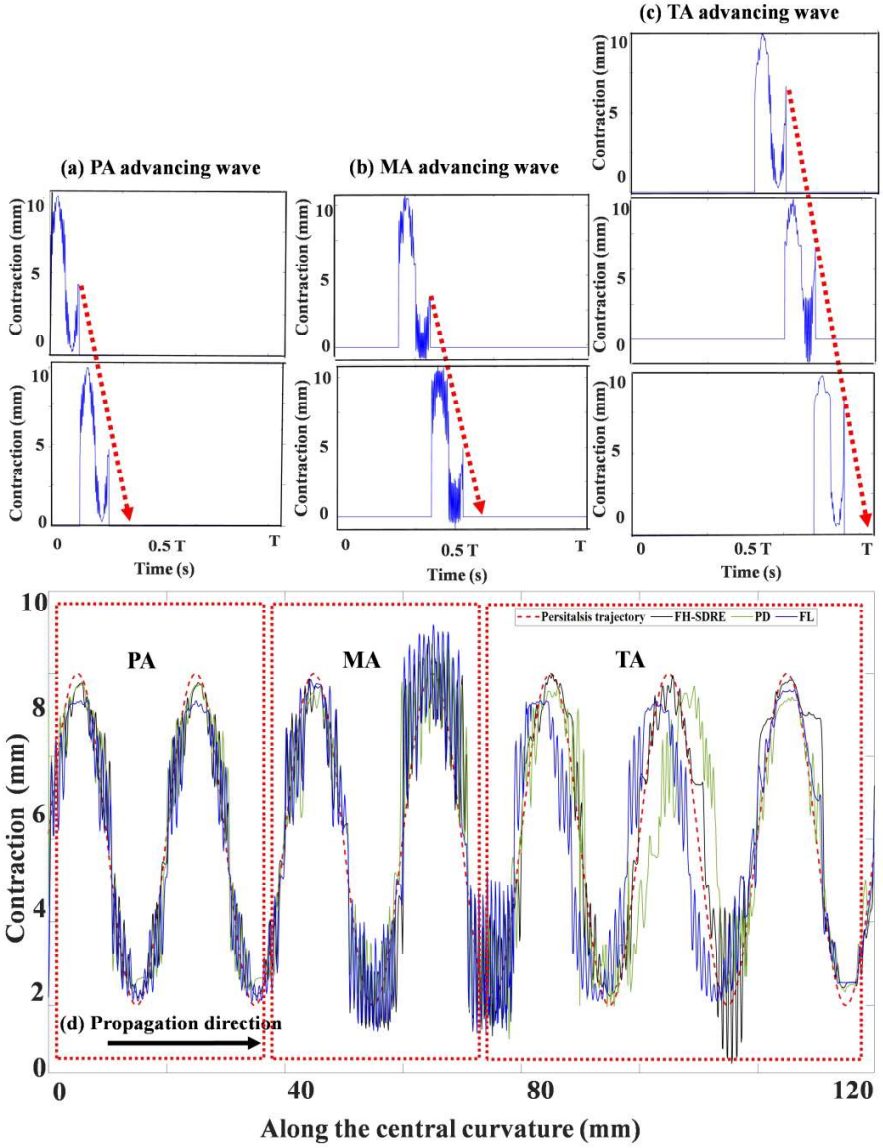

Fig. 8. The experimental results showing the propagation of the contraction over time. **(a-c)** The advancing wave in each segment of the gastric simulator including PA, MA, and TA. **(d)** The according peristalsis throughout the entire antrum in T= 20 seconds. Each zone has a repeated contraction three times. In **(d)**, the red-dashed line is the peristalsis trajectory, the blue, green and black lines are the actual output of the robot following the baseline under FL, PD, and FH-SDRE control respectively. Note that to the detailed controllers' results are presented quantitatively in Table 4. The initial position in each segment is the neutral position 6 mm). As mentioned in Table 2, the number of sensors for PA and MA is two, and for the TA is three. That is why TA has one more trajectory compared to the other two segments.

739x956mm (96 x 96 DPI)

Table 4. The analysis of the experimental tracking trajectory of the gastric simulator under different controllers.

Controller	The average of three segments		PA		MA		TA	
	Mean RMSE (mm)	Mean control norm	RMSE (mm)	Control norm	RMSE (mm)	Control norm	RMSE (mm)	Control norm
FL	1.26	506.86	0.69	334.88	1.17	597.91	1.94	587.79
FH-SDRE	0.8	411.39	0.64	298.72	0.98	483.74	0.77	451.71
PD	2.1	257.73	0.64	135.04	1.36	293.11	4.49	345.06

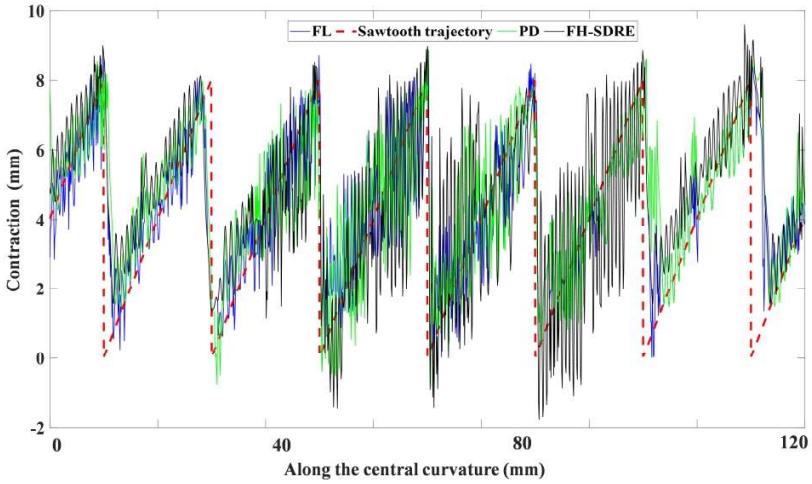

Fig. 9. Tracking the sawtooth trajectory by the gastric simulator under PD, FH-SDRE, and FL controllers.

1164x619mm (96 x 96 DPI)

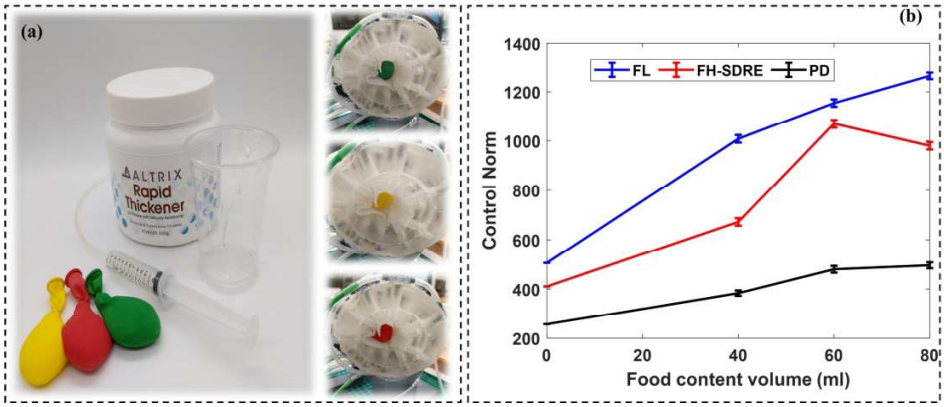

Fig. 10. The experimental test with food content. **(a)** Preparation of the honey-like fluid balloons and squeezing them into the robot. According to its instruction, ten scoops of thickener must be mixed with 1.0 L water to obtain a honey-like viscosity. **(b)** The graph regarding three different closed-loop controllers illustrating the increase in control effort with the increase in the volume of the food content. The numbers are the average of ten times experiments (see the standard deviation). Note that the food contents were wrapped in balloons to avoid the stains or remains of the food content affecting the validation of the gastric simulator over several experiments.

756x315mm (96 x 96 DPI)

Fig. 1. **(a)** Internal view of the stomach muscles with different textures. **(b)** The stomach has five regions, including the gastroesophageal junction (cardia), the fundus, the body (corpus), the antrum, and the pylorus.[37,38] Note that despite the blue-dashed lines, the antrum is not easily distinguishable with the boundary between the corpus and the antrum difficult to visually delineate. Also, the schematic of the stomach shows different sections of the antrum. **(c)** 3D projections of the designed stomach simulator in CAD. Different projections of the CAD design of the inner mold for the conduit and the outer mold with bellows.

Fig. 2. **(a)** 3D-design and print of the molds. Hot glue gun was used to seal the seams between the 2-pieces molds when the uncured elastomer (Ecoflex 00-30 and Slacker; Smooth-on, Inc.), was poured inside the assemblies. Elastomer mix were Ecoflex (1A:1B) and PDMS (1 curing agent:10 PDMS (Sylgard 184 silicone elastomer; DOW)) similar to previous work.[16,35] Slacker™ was added to Ecoflex mix to change the "feel" of the silicone rubber to a softer and more "flesh-like" material by 0.5. Sil-Poxy™ (Sil-Poxy; Smooth-on, Inc.) is an adhesive for bonding different soft parts together. **(b)** The process of producing sensor caps, in which PDMS was used as it is clearer than Ecoflex. **(c)** The final assembled/sealed gastric simulator showing the side and front (PA), the pneumatic tubes and fittings, and the comparison with an actual antrum.

Fig. 3. **(a)** The connection between VCNL4040, multiplexer, myRIO and the PC. VCNL4040 has a unique device address (slave address), 0x60 (HEX), so myRIO can choose which devices will be communicating through two sensor wires. The two wires are the serial clock (SCL) and serial data (SDA). The SCL line is the clock signal that synchronizes the data transfer between the devices on the I^2C bus and is generated by the master device, and the other line, SDA, carries the data. TCA9548A multiplexer (outside of the gastric simulator attached to myRIO through wires) can get up to eight same slave address I^2C sensors communicating to one microcontroller. **(b)** The attachment of the sensors on the top of sensor caps and their placement on the gastric simulator using silicon glue, and the calibration graph of the sensors. Note that a lowpass filter is added to reduce the sensor noises.

Fig. 4. Schematic of the electro-pneumatic system. For the pressurized state, electro-pneumatic regulators (ITV0030, SMC), pressure regulator, and for the vacuum state electronic vacuum regulators (ITV0090, SMC), vacuum regulator, are used. The relationship between the input signal and the pressure/vacuum outputs is linear in both ITV0030 and ITV0090. The pressure range for the vacuum and pressure regulators is -100 and 500 kPa, respectively. For the switching state, a micro-3-port solenoid valve (005 series, KOGANEI) is use. NI myRIO acts as an integration unit to merge the sensory and pneumatic parts into one entity and process all the data, controller, and feedback through LabVIEW scripts.

Fig. 5. The algorithms of **(a)** sequencing, **(b)** multiplexer and sensor readings, **(c)** and their connection to the regulator commands. In Electro-pneumatic unit section, it was explained that each regulator and solenoid was connected to a specific myRIO pin, including analog output, PWM, and digital input/output. Solenoid acts as a switch between pressure and vacuum regulators.

Fig. 6. (a) The sample of a RiSPA with five bellows. For the bellows' arrangement, they are scattered over the conduit uniformly without colliding.[16] The angle between the bellows is $2\alpha = 360/n$, where n is the number of bellows in a RiSPA. **(b)** The schematics of a RiSPA and its model characteristics, where $r_i(t)$ and $\theta_i(t)$, ($i = 1, ..., n$), are radial and lateral movements of the ith-bellows in the cross-section plane.

Fig. 7. (a) The flowchart of the numerical simulation (regulation process) to determine the weighting matrices for both the FL and FH-SDRE. **(b)** The flowchart of the numerical simulation (regulation process) to determine the control gains for the PD. **(c)** The implementation logic (block diagram) of the controllers on the presented gastric simulator.

Fig. 8. The experimental results showing the propagation of the contraction over time. **(a-c)** The advancing wave in each segment of the gastric simulator including PA, MA, and TA. **(d)** The according peristalsis throughout the entire antrum in T= 20 seconds. Each zone has a repeated contraction three times. In **(d)**, the red-dashed line is the peristalsis trajectory, the blue, green and black lines are the actual output of the robot following the baseline under FL, PD, and FH-SDRE control respectively. Note that to the detailed controllers' results are presented quantitatively in Table 4. The initial position in each segment is the neutral position 6 mm). As mentioned in Table 2, the number of sensors for PA and MA is two, and for the TA is three. That is why TA has one more trajectory compared to the other two segments.

Fig. 9. Tracking the sawtooth trajectory by the gastric simulator under PD, FH-SDRE, and FL controllers.

Fig. 10. The experimental test with food content. **(a)** Preparation of the honey-like fluid balloons and squeezing them into the robot. According to its instruction, ten scoops of thickener must be mixed with 1.0 L water to obtain a honey-like viscosity. **(b)** The graph regarding three different closed-loop controllers illustrating the increase in control effort with the increase in the volume of the food content. The numbers are the average of ten times experiments (see the standard deviation). Note that the food contents were wrapped in balloons to avoid the stains or remains of the food content affecting the validation of the gastric simulator over several experiments.